AGU ADVANCING EARTH AND SPACE SCIENCE

Geophysical Research Letters®

RESEARCH LETTER
10.1029/2022GL101306

Revealing Crustal Deformation and Strain Rate in Taiwan Using InSAR and GNSS

Kathryn R. Franklin[1] **and Mong-Han Huang**[1]

[1]Department of Geology, University of Maryland, College Park, MD, USA

Abstract Interseismic deformation describes the gradual accumulation of crustal strain within the tectonic plate and along the plate boundaries before the sudden release as earthquakes. In this study, we use 5 years of high spatial and temporal geodetic measurements, including Global Navigation Satellite System and Interferometric Synthetic Aperture Radar to monitor 3-dimension interseismic crustal deformation and horizontal strain rate in Taiwan. We find significant deformation (strain rate $>8 \times 10^{-6}$ yr^{-1}) along the plate boundary between the Philippine Sea and the Eurasian Plates in east Taiwan. The high strain rate in the southern part of the Western Foothills is distributed along a few major fault systems, which reveals the geometry of the deformation front in west Taiwan. Our results help identify active faults in southwest and north Taiwan that were not identified before. These findings can be insightful in informing future seismic hazard models.

Plain Language Summary An earthquake cycle includes three phases: interseismic, coseismic, and postseismic. Interseismic deformation refers to the continuous crustal deformation that is built up by active tectonics. Depending on the relative motion between tectonic plates, the earthquake recurrence interval could vary by a few orders between different locations. As a result, knowing the crustal deformation rate and deformation accumulated in different fault zones can be useful for investigating future earthquake hazards. Using space geodesy tools like Global Navigation Satellite System and Interferometric Synthetic Aperture Radar, we can monitor surface deformation during the interseismic period. In this study, we monitor interseismic deformation in Taiwan using geodesy. We find that east Taiwan where two tectonic plates collide has the highest rate of deformation. In southwest and north Taiwan where most of the population resides, there is also high-level of deformation distributed across a few different faults, indicating that some of the faults have a higher risk generating future earthquakes. As a result, knowing the amount of faults slip and amount of deformation built up during this interseismic period may inform us of potential future earthquake hazards.

Key Points:

- This study combines Interferometric Synthetic Aperture Radar and Global Navigation Satellite System and produces high-resolution 3-D interseismic crustal velocities and strain rate estimates in Taiwan
- Strain rate measurements show high surface strain cumulation along east and southwest Taiwan
- The surface strain rates and the earthquake hazard models based on seismology and field study are in good agreement

Supporting Information:

Supporting Information may be found in the online version of this article.

Correspondence to:

M.-H. Huang,
mhhuang@umd.edu

Citation:

Franklin, K. R., & Huang, M.-H. (2022). Revealing crustal deformation and strain rate in Taiwan using InSAR and GNSS. *Geophysical Research Letters*, *49*, e2022GL101306. https://doi.org/10.1029/2022GL101306

Received 23 SEP 2022
Accepted 10 OCT 2022

Author Contributions:

Conceptualization: Kathryn R. Franklin, Mong-Han Huang
Data curation: Kathryn R. Franklin
Formal analysis: Kathryn R. Franklin, Mong-Han Huang
Funding acquisition: Mong-Han Huang
Investigation: Kathryn R. Franklin, Mong-Han Huang
Methodology: Kathryn R. Franklin, Mong-Han Huang
Software: Mong-Han Huang
Supervision: Mong-Han Huang
Validation: Kathryn R. Franklin, Mong-Han Huang

1. Introduction

Taiwan is located between the Eurasian Plate and the Philippine Sea Plate. The Philippine Sea Plate moves toward northwest with a rate of >80 mm/yr and causes an oblique collision with the Eurasian Plate (Lin et al., 2010; Yu et al., 1997). This collisional tectonics has given rise to a few geologic provinces, including (from west to east) Coastal Plain (CP), Western Foothills (WF), Hsueshan Range (HR), Central Range (CR), Longitudinal Valley (LV), and the Coastal Range (CoR) (Figure 1a). The high collision rate has resulted in a large number of earthquakes in Taiwan, and several devastating events have been located in west Taiwan where the majority of the population resides.

Interseismic deformation describes the gradual accumulation of crustal strain within the tectonic plate and along the plate boundaries before its sudden release as earthquakes. Global Navigation Satellite Systems (GNSS) and InSAR have been widely used to quantify the interseismic crustal deformation (Elliott et al., 2016). The high convergence rate in Taiwan is among the highest in the world and suggests significant elastic strain accumulation in a relatively short period of time (Figure 1b).

Although Taiwan has one of the highest GNSS network densities in the world, GNSS measurements alone still could not confidently identify interseismically creeping faults when they are not close to these faults. For example, a GNSS-based dilatation rate map (Figure 1c) highlights regions undergoing interseismic contraction in east and southwest Taiwan and extension in northeast Taiwan in a broader scale, but it remains challenging to identify active faults or to determine interseismic fault slip for closely spaced faults. Alternatively, InSAR provides high spatial resolution measurements of surface deformation at a cm-level accuracy level (Bürgmann et al., 2000;

Visualization: Kathryn R. Franklin
Writing – original draft: Kathryn R. Franklin, Mong-Han Huang
Writing – review & editing: Mong-Han Huang

Elliott et al., 2016). Recent work (e.g., Shen & Liu, 2020; Tong et al., 2013; Weiss et al., 2020) combines GNSS and InSAR to achieve a high spatial resolution with relatively high accuracy. This method is done by utilizing GNSS for the long-wavelength spatial deformation and InSAR for short-wavelength features. Huang and Evans (2019) estimated crustal deformation in southwest Taiwan between 2005 and 2009 using InSAR-GNSS combined data and were able to characterize fault slip and locking depth of the major fault system using a total variation regularization approach for southwest Taiwan. However, their work does not include other active deforming regions such as east Taiwan.

In this study, we employ GNSS and InSAR data to generate 3-D interseismic velocities in Taiwan based on data collected between 2016 and 2021. In application, we highlight surface deformation patterns using high resolution 3-D velocities and produce a horizontal strain rate analysis to identify interseismically active faults that can help produce better future seismic hazard models.

2. Data and Method

2.1. SAR and GNSS Data Collection

The Synthetic aperture radar (SAR) data were obtained from the European Space Agency (ESA) Sentinel-1 mission for the Copernicus initiative. This mission collects C-band SAR acquisitions with a wavelength of ~55.5 mm and provides single-look complex (SLC) products. In this study, we used Sentinel-1 SAR acquisitions from ascending track 69 and descending track 105 between November 2016 and July 2021. We do not include SAR data before November 2016 to avoid coseismic deformation and to reduce early postseismic deformation of the 2016 M_W 6.4 MeiNong earthquake in southwest Taiwan (e.g., Huang, Tung, et al., 2016). However, our observation period includes the 2018 M_W 6.4 Hualien earthquake in northeast Taiwan (Huang & Huang, 2018). This is because there is sufficient number of InSAR acquisitions before the Hualien earthquake and the epicenter is

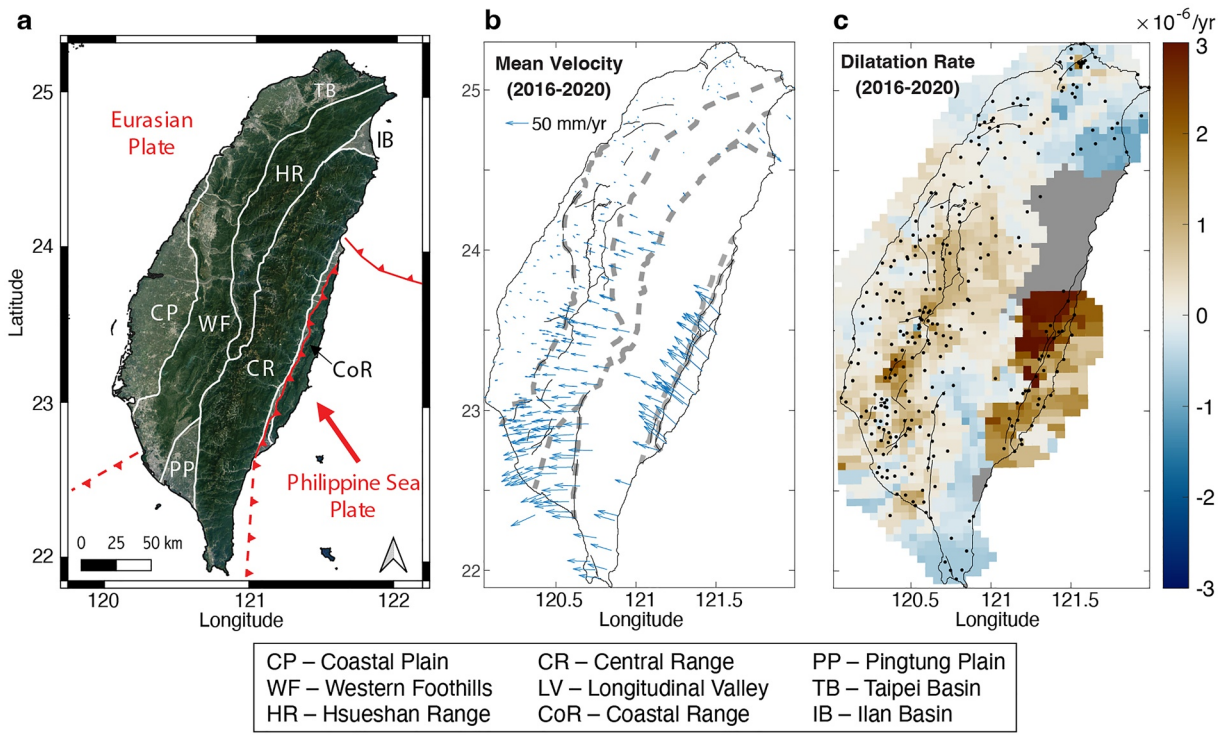

Figure 1. Tectonic setting and crustal deformation of Taiwan. (a) The solid and dashed red lines indicate plate boundaries. The white lines indicate geologic province boundaries. The full name of each geologic province and location is shown below the figure. (b) Mean Global Navigation Satellite System (GNSS) velocities between 2016 and 2021 from this study. The black lines are active faults identified by CGS (2021). (c) Dilatation rate based on GNSS data in (b). Black dots are GNSS stations used for the analysis. Gray color represents areas without strain rate results due to lower GNSS network density. Red and blue represent contraction and extension rate (in 10^{-6} yr^{-1}), respectively.

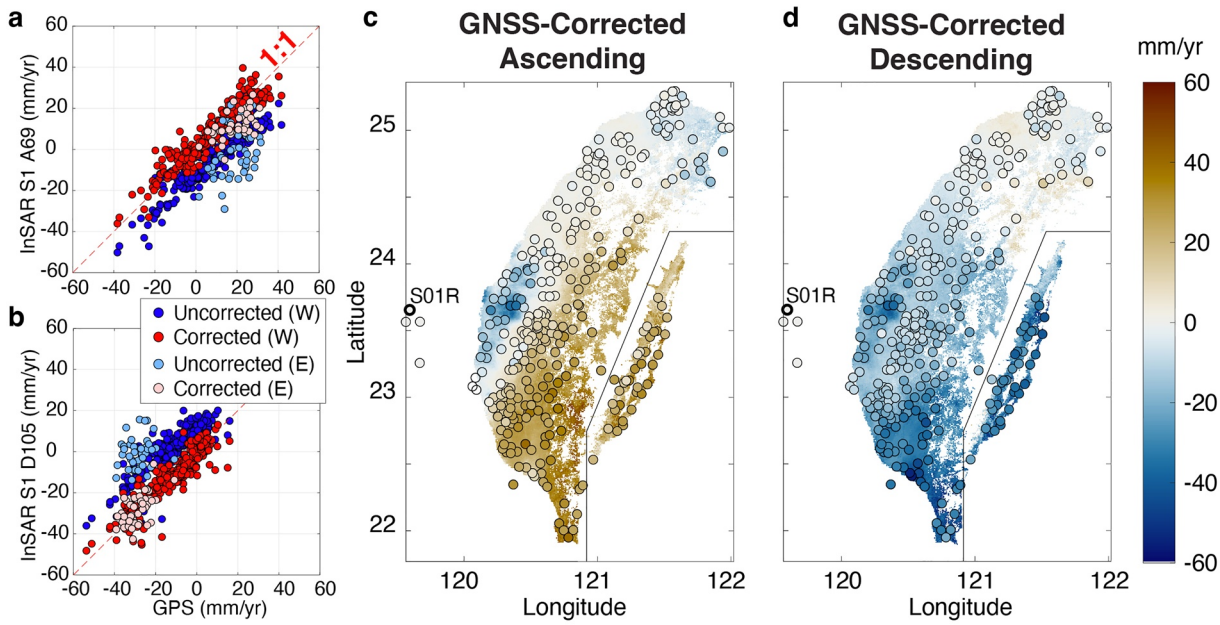

Figure 2. Comparison of Interferometric Synthetic Aperture Radar (InSAR) and Global Navigation Satellite System (GNSS) velocities. Comparison of velocities before and after correction for ascending (a) and descending (b) tracks. The red dash line in (a) and (b) represents a 1:1 ratio between GNSS and InSAR. W and E in (a) and (b) represent west and east Taiwan, respectively. Positive and negative values in (c) and (d) represent movement toward and away from the satellite line-of-sight, respectively. S01R in (c) and (d) is the reference GNSS station.

offshore. We estimate the coseismic and postseismic components of the Hualien earthquake from the time series analysis (Supporting Information S1).

Digital elevation models (DEM) were downloaded from NASA Jet Propulsion Lab's Shuttle Radar Topography Mission with 30 m resolution and 1-arc s (Farr et al., 2007), which is stored in the USGS Measures project. The DEM data were used to remove elevation contributions to phases in InSAR images. The weather model used in the troposphere noise correction was downloaded from European Centre for Medium-Range Weather Forecasts (ECMWF) Reanalysis fifth Generation weather model products (Hersbach et al., 2020).

The continuous GNSS time series data are processed and maintained by the Central Geologic Survey (CGS), the Central Weather Bureau, the Ministry of Interior, Taiwan, and the GPS Laboratory at the Institute of Earth Science, Academia Sinica, Taiwan. The data are accessed from Academia Sinica, Taiwan. Additionally, each GNSS station time series was adjusted to remove common network offsets unrelated to crustal deformation. All the GNSS velocities are relative to station S01R on Penghu Island (Figure 2c). Similar to the InSAR observation time period, we do not include the GNSS time series before November 2016 in order to reduce contribution from the 2016 MeiNong earthquake. As for the 2018 Hualien earthquake, we do not include GNSS stations within 50 km from the earthquake epicenter in the GNSS analysis.

2.2. InSAR Time Series Processing

The InSAR products were processed using InSAR Scientific Computing Environment (ISCE) software developed at NASA JPL Caltech (Rosen et al., 2012). The TOPS Stack Processor is a module of the ISCE software package that enables SAR images to be combined to generate InSAR images (Fattahi et al., 2017), including applying phase unwrapping using Snaphu (Chen & Zebker, 2002). We used the Stack Sentinel module to generate SAR acquisition pairs by taking orbital data, DEM data, bounding box, auxiliary data (Sentinel-1 instrument parameters), the number of adjacent SAR images to be processed and the start and end dates into account. We take a network of three of adjacent SAR acquisitions in the stack processing.

We used the *Miami InSAR Time Series Software in Python* (Mintpy) (Yunjun et al., 2019) to generate InSAR time series. Mintpy applies tropospheric noise corrections using the ECMWF weather model and generates the time series. We then estimate mean line-of-sight (LOS) velocities based on the ascending and descending InSAR time series.

Mintpy uses a small baseline subsets approach to find the best fitting time series for the given interferograms while minimizing the implied velocities (Bernardino et al., 2002). To avoid phase unwrapping errors due to steep mountain ranges and dense vegetation in the Central Range (CR in Figure 1a) that could generate a phase offset between west and east Taiwan, we separate the island into west and east Taiwan and perform phase unwrapping separately. Since each part has its own reference point, we merge InSAR results in east and west Taiwan onto a GNSS reference frame.

2.3. Generation of 3-D Velocities

Here we briefly document the process of retrieving mean velocities from InSAR and GNSS time series (see Supporting Information S1 for more details). This process estimates mean velocities from the ascending and descending LOS time series using a polynomial function fit for each InSAR pixel and GNSS station (e.g., Figure S1 in Supporting Information S1). To adjust InSAR velocities to the GNSS reference frame, we first calculate GNSS velocities in InSAR ascending and descending LOS from the 3 components (east-west, north-south, and vertical). For each GNSS station, we use InSAR pixels within 500 m distance from the GNSS station to estimate the average InSAR velocity at the GNSS station in order to reduce InSAR phase noise. As shown in Figures 2a and 2b, besides a consistent shift between InSAR and GNSS velocities, InSAR and GNSS results are quite consistent. This is shown by a trend shifted from the 1:1 line between InSAR and GNSS data distribution (blue circles in Figure 2c) due to different reference points between GNSS and InSAR. We use a least square approach to fit InSAR into GNSS-simulated LOS (red circles in Figure 2c). After this adjustment, we interpolate GNSS velocities to InSAR samplings using *cubic* interpolation in Matlab. Once this is done, we use the equations that relate LOS and 3-D components for both InSAR and GNSS, and calculate 3-D velocity of each InSAR pixel through a least square inversion. Although the velocity estimates between GNSS and InSAR could be different, the root-mean-square difference between GNSS and InSAR is 4.6 mm/yr for ascending and 4.9 mm/yr for descending track. We therefore consider high consistency between the two datasets.

3. 3-D Interseismic Velocities

The 3-D surface deformation results are shown in Figure 3, and the associated uncertainties are shown in Figures S2 and S3 in Supporting Information S1. We consider the mean velocity results to be representative of the interseismic crustal velocities in Taiwan since we have removed contribution from major earthquakes. In the horizontal components, the north-south motion is smoother because it is mostly constrained by the interpolated GNSS data, since InSAR has lower sensitivity to north-south motions. There are no estimated velocities along the east side of the Central Range (CR in Figure 1a) because of the high topographic relief that decreases the coherence in most interferograms. The 3-D velocities show up to 40 mm/yr southwestward motion in southwest Taiwan. In east Taiwan, there is >40 mm/yr northwestward motion along the LV Fault (LVF) in Figure 3b. There is observable surface subsidence in the north Coastal Range (CoR in Figure 1a), whereas there is more than 20 mm/yr of uplift in the south CoR, which is similar to finding by Hsu and Bürgmann (2006). Along the CR, there is up to 20 mm/yr uplift. In the Coastal Plain (CP in Figure 1a), there is more than 40 mm/yr surface subsidence due to anthropogenic groundwater pumping (Huang, Bürgmann et al., 2016; Hung et al., 2010, 2011; Tung & Hu, 2012).

In transect A (Figure 3d), there is an up to 20 mm/yr increase of horizontal motion across the Milun Fault (MF in Figure 3d). However, this motion could be associated with the 2018 Hualien earthquake that significant slip along the Milun Fault (Huang & Huang, 2018), and the postseismic contribution in the InSAR time series may not be entirely removed. The vertical motion is relatively stable in the WF, followed by a total of 17 mm/yr of uplift in the HR that could potentially be associated with slip along the main detachment fault below CR (Ching et al., 2011).

Along transect B (Figure 3e), the horizontal velocity increases by 40 mm/yr from CP to west CR, followed by another rapid increase (20 mm/yr) across LVF. In the vertical component, there is >40 mm/yr of surface subsidence likely due to anthropogenic activities. The uplift rate gradually increases from WF to CR with a peak uplift rate ~15 mm/yr, which is similar to the long-term uplift rate in Taiwan based on exhumation rate measurements of rocks (e.g., data synthesized by Ching et al., 2011). There is ~10 mm/yr of subsidence in the LV between CR and CoR. The clear horizontal and vertical velocity offset along LVF suggest shallow fault creep (Champenois et al., 2012; Lee

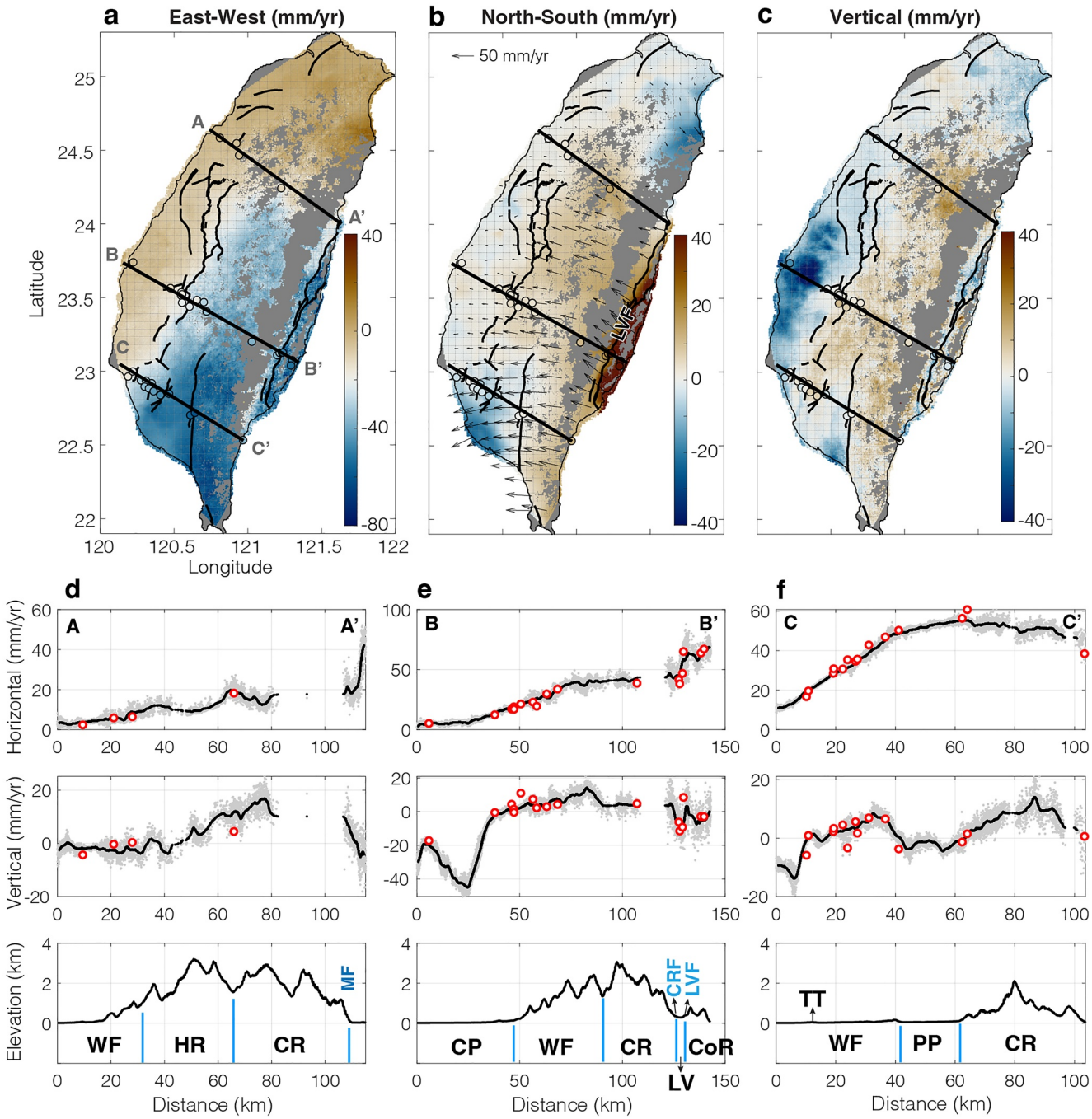

Figure 3. 3-D velocities based on the InSAR-GNSS combined data set. (a) East-West, (b) North-South, and (c) Vertical velocities. Note the color scale in (a) is different from (b) and (c). The arrows in b show the horizontal velocities relative to station S01R (Figure 2c). Positive values represent eastward, northward, or upward motions. The black lines are active faults identified by CGS (2021). The colored circles are Global Navigation Satellite System (GNSS) stations plotted in the transects. (d), (e), and (f) are three selected transects across the island. In each subplot, the top and middle rows are the horizontal (square root of the east-west and north-south components) and vertical components, respectively. The gray dots are Interferometric Synthetic Aperture Radar (InSAR) horizontal or vertical velocities, with the black lines representing the smoothed velocities (smoothing widow size is 100 pixels). The red circles are GNSS mean velocity along the same transect. The bottom of each subplot shows surface topography. The vertical blue lines indicate the geologic boundaries. TT is the location of the Tainan Tableland, and the other abbreviations are the same as those in Figure 1.

et al., 2005). Although there is a clear vertical offset along the Central Range Fault (CRF), a lack of horizontal offset across CRF implies the subsidence in LV here could be due to anthropogenic activity. The location of transect B is similar to that presented in both Ching et al. (2011) and Hsu et al. (2018). While the horizontal component is similar to that in Ching et al. (2011), the vertical component is more similar to Hsu et al. (2018).

Transect C (Figure 3d) goes across the most active structure of WF. There is ∼50 mm/yr of increase in horizontal velocity from west to east WF. The velocity starts to decrease by ∼3 cm/yr from west to east CR. In the vertical component, there is subsidence west of the Tainan Tableland (TT) in Figure 3f, likely related to anthropogenic groundwater pumping. We find clear uplift in WF and CR, but close to no vertical motion in the Pingtung Plain (PP) in Figure 1a.

4. Strain Rate Analysis

We calculate the strain rate tensor of Taiwan from the InSAR-GNSS combined data set. Since surface displacements associated with major earthquakes were removed, we consider this data set representing the interseismic deformation of Taiwan. To reduce computation time, we first downsample the horizontal velocities to 500 m pixel spacing. Since strain rate is differential velocities of pixels divided by pixel distance, it could dramatically amplify short-wavelength noise in InSAR and make the result uninterpretable. For example, 1 mm of noise in 1-D velocity between two pixels 500 m apart can cause longitudinal strain equivalent to 2×10^{-6}. We therefore consider using a group of pixels within a characteristic distance for constructing the strain rate tensor of each grid point. To explore the appropriate length scale of the smoothing, we use a semi-variogram approach suggested by Sudhaus and Jónsson (2009) in a region that is stable in west Taiwan (Text S2 in Supporting Information S1). We estimate spatially correlated signals in the horizontal velocities and find a characteristic distance of ∼7 km (Figure S6 in Supporting Information S1). Based on this value, when we generate the strain rate tensors we take into account velocities of 144 nearby pixels of each grid point. This number is obtained from the number of pixels that occupy a circular area with 3.4 km radius and 500 m pixel spacing.

The dilatation and the second invariant of the strain rate with 1 km grid spacing are shown in Figure 4. To reduce the complexity of the fault naming system, we use fault ID numbers consistent with CGS in Taiwan (CGS, 2021) and use the fault ID number than fault names for most of the time hereafter. The fault names are listed below Figure 4f. The dilatation rate from the InSAR-GNSS data set (Figure 4a) has much higher spatial resolution than the GNSS-only results (Figure 1c). In east Taiwan, the dilatation rate shows a very localized deformation along LVF. In west Taiwan, we find higher contraction rate within WF, along several major faults (black fault lines in Figure 4b). The distribution of the high second invariant may reveal the deformation front of west Taiwan. In north Taiwan (Figure 4c), there is a clear extension in Ilan (IL). We also find a localized extension in the south side of Taipei (TP in Figure 4c).

The second invariant of the strain rate tensor (Figure 4d) shows the total amount of strain rate (both dilatation and shear). Similar to the dilatation rate, the highest deformation is along LVF with rate $>8 \times 10^{-6}$ yr^{-1}. Southwest Taiwan has the next highest strain rate after LVF. In a detailed view (Figure 4e), there is increased deformation along the major faults (labeled in numbers in Figure 4e). This result provides much better spatial resolution of deformation than the GNSS-only products (Figure 1c). We additionally find higher strain rate along faults that were not considered active by CGS (2021) but were identified by Chen (2016) based on fieldwork and paleoseismology (indicated by the dashed lines in Figures 4b, 4c, 4e, and 4f). In northern Taiwan, in addition to fault ID 39 (or F39), we also find higher deformation in the north and south sides of IL (F40 and F41).

5. Comparing With Seismic Hazard Models

Chan et al. (2020) provided the 2020 version of the Taiwan Earthquake Model (TEM) of Probabilistic Seismic Hazard Analysis (PSHA) following an initial model built by Wang et al. (2016) and fault information by Shyu et al. (2016, 2020). The TEM PSHA model estimates seismic hazard based on a seismogenic structure database, an updated earthquake catalog, time-dependent rupture model, and a revised area source model to estimate the seismic hazard map of Taiwan. With incorporation of Vs30 (shear-wave velocity in the top 30 m depth) for calculating site amplification, the TEM PSHA model identified a few fault structures with an increased seismic hazard potential close to the IB, LV, and southwest WF (see Figure 1a for locations). In this section we compare the TEM PSHA model (called *seismic hazard model* hereafter) that predicts future earthquake probability, with the second invariant of the strain rate tensor, which highlights the mean surface strain rate magnitude between 2016 and 2021. Although they do not need to agree, regions with higher interseismic strain accumulation tend to be more seismically active.

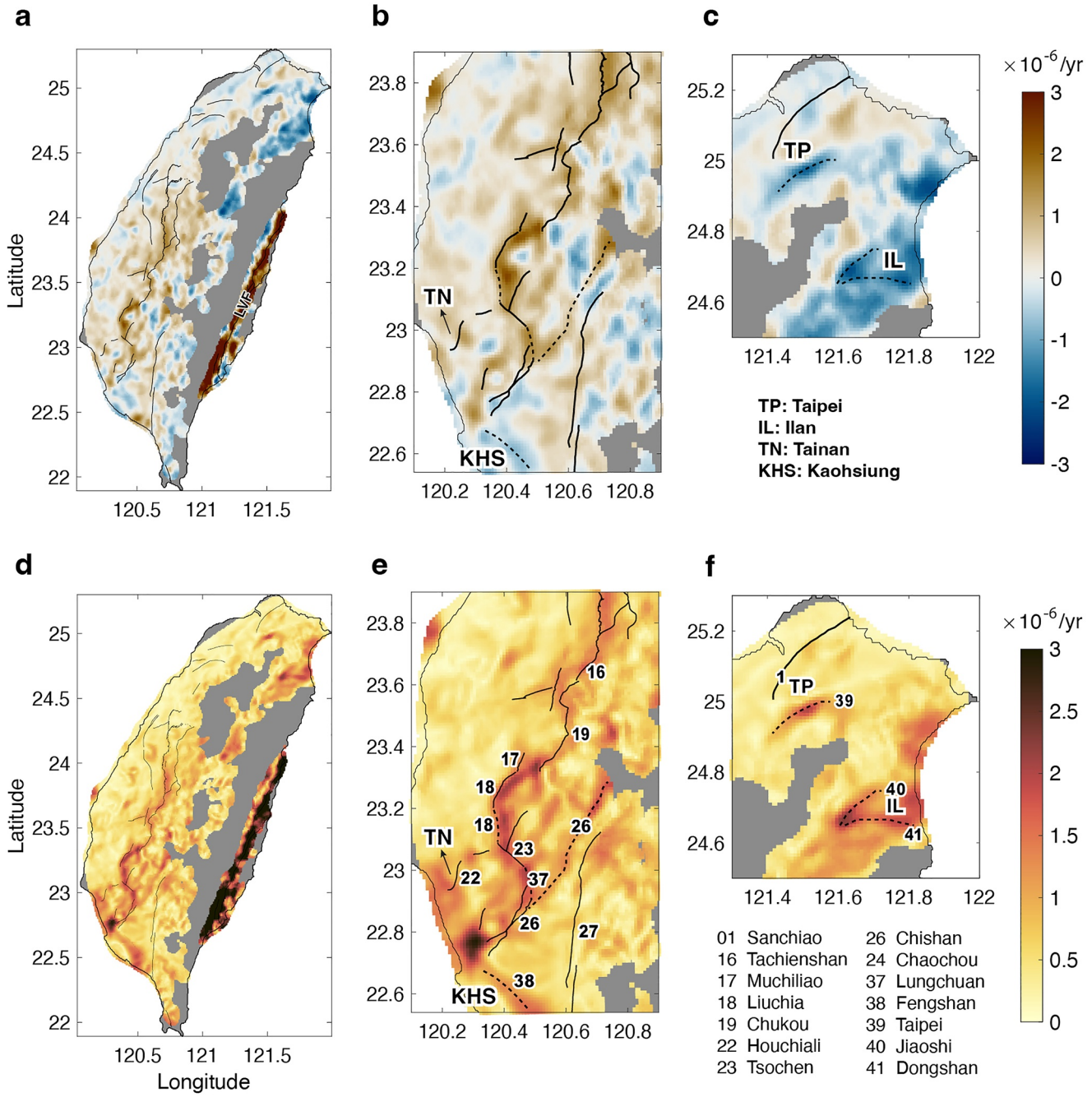

Figure 4. InSAR-GNSS combined strain rate in Taiwan. (a) Dilatation rate. Warm and cold colors indicate contraction and extension, respectively. The color scale is shown in (c). (b) and (c) show the dilatation rate in southwest and north Taiwan, respectively. (d) Second invariant of the strain rate tensor. Warmer color indicates a higher strain rate magnitude. The color scale is shown in (f). (e) and (f) show the second invariant in southwest and north Taiwan, respectively. The black lines in each plot are the active fault traces identified by CGS (2021). In (b) and (c), Tainan (TN), Kaohsiung (KHS), Taipei (TP), and Ilan (IL) are cities (names listed below c). The dashed lines in (b), (c), (e), and (f) are potentially active faults based on strain rate analysis. The numbers in (e) and (f) are faults with names listed below (f). Naming of F37-41 is based on Chen (2016).

We find some similarity between the seismic hazard model and the second invariant of the strain rate tensor. In southwest Taiwan where interseismic strain rate is higher (Figure 4e), both F17 and F18 have high seismic potential in the seismic hazard model. However, the distribution of high seismic potential south of F18 is different, where high strain rate diverts into F37 and F22. F22 is in east TT with an estimated ~10 mm/yr creep rate from previous studies (e.g., Huang et al., 2006; Le Béon et al., 2019), but here we additionally find surface deformation

west of Tainan (TN). Further to the southwest side of F26 and along F38, the seismic hazard map does not predict a particularly high seismic probability, whereas high interseismic strain rate is observed. The high strain rate between F22, F26, and F38 could be of concern because TN and Kaohsiung, the two major cities, are located nearby the fault structures.

In north Taiwan, both the second invariant (Figure 4f) and the seismic hazard model show higher deformation and higher seismic probability in Ilan (IL). In Taipei (TP), the capital city of Taiwan, we observed extension strain rate of $\sim 2 \times 10^{-6}$ yr^{-1} along F39, while the seismic hazard model does not predict a higher hazard potential. F39 (TP Fault) has been identified as an inactive reverse fault, but earthquake focal mechanisms near this region show a sign of extension (Teng et al., 2001). There is also a clear surface subsidence in the TP (Figure 3c) because of groundwater pumping which can induce soil compaction, aquifer deformation, and general subsidence (Chen et al., 2007). We cannot discern whether fault creep could have contributed to the surface subsidence near F39. Future studies on seasonal variation of surface movement and how it relates to precipitation and groundwater discharge data may provide further insight into identifying the cause of surface subsidence in this time period.

Again, interseismic surface strain rates do not have to agree with seismic hazard models because they do not inform coseismic displacement. A better knowledge of interseismic fault slip, fault locking depth, and detection of active faults may provide significant contributions in advancing fault geometry and slip models for the seismic hazard models. For example, the second invariant result identifies additional faults that are currently active but are not identified as active faults possibly due to limited field mapping or a lack of seismicity during aseismic fault creep, hence not detected using seismology. Future interseismic fault slip models with geodetic constraints can further incorporate fault slip budget (Avouac, 2015). Probabilistic earthquake likelihood models using both geodetic measurements and seismic catalog (e.g., Rollins & Avouac, 2019) may provide insightful contribution to future seismic hazard models.

6. Conclusions

Combining the capabilities of GNSS and InSAR, we can better reveal interseismic crustal deformation of Taiwan. Through a series of GNSS and InSAR comparisons, we find consistency between the two datasets. The InSAR-GNSS combined result shows greater deformation in east and southwest Taiwan, and there is >40 mm/yr of surface subsidence in west Taiwan due to anthropogenic water pumping and up to 20 mm/yr of uplift in the CR. Strain rate analysis suggests $>8 \times 10^{-6}$ yr^{-1} surface contraction rate along the LV Fault, and there is also a higher level of contraction in the southwest WF. The high-resolution strain rate results may reveal the distribution of the deformation front of Taiwan. Our work demonstrates a high spatial resolution of surface deformation that can be revealed by publicly available SAR data with open-source processing tools. Our results highlight creeping faults in east and southwest Taiwan and help identify active faults that were not identified before. These findings can be useful for informing future seismic hazard models.

Data Availability Statement

The SLC products containing the SAR images were downloaded from the Alaska Satellite Facility (ASF) (https://search.asf.alaska.edu/%23/). Readers can specify Taiwan as area of interest and time of interest (2016–2021 and paths 69 & 105) to acquire SLC products used in this study. The precise orbital data of the Sentinel-1 satellites were downloaded from ESA Science Hub (https://scihub.copernicus.eu/). Readers can specify 2016 to 2021 as sensing period and download the AUX_POEORB products used in this study. The stack process is part of the ISCE InSAR processing software package (Rosen et al., 2012). Mintpy is an open-source InSAR time series processing software (Yunjun et al., 2019). The InSAR-GNSS data set and the strain rate results can be found in the Supplementary Data set. They are also archived in Zenodo (https://doi.org/10.5281/zenodo.7193858).

Acknowledgments
We want to thank Eileen Evans, Chung Huang, Vedran Lekić, and Laurent Montesi for their insightful comments on the original manuscript. MH thanks Kathrine Udell Lopez for proofreading the manuscript. Editor Lucy Flesch, Tim Byrne, and an anonymous reviewer provide valuable comments. We also thank the GPS laboratory at the Academia Sinica in Taiwan who actively maintains the GNSS stations. This work is supported by NSF EAR-2026099.

References

Avouac, J.-P. (2015). From geodetic imaging of seismic and aseismic fault slip to dynamic modeling of the seismic cycle. *Annual Review of Earth and Planetary Sciences*, *43*(1), 233–271. https://doi.org/10.1146/annurev-earth-060614-105302

Bernardino, P., Fornaro, G., Lanari, R., & Sansosti, E. (2002). Monitoring based on small baseline differential SAR interferograms. *IEEE Transactions on Geoscience and Remote Sensing*, *40*(11), 2375–2383. https://doi.org/10.1109/tgrs.2002.803792

Bürgmann, R., Rosen, P. A., & Fielding, E. J. (2000). Synthetic aperture radar interferometry to measure Earth's surface topography and its deformation. *Annual Review of Earth and Planetary Sciences*, *28*(1), 169–209. https://doi.org/10.1146/annurev.earth.28.1.169

Central Geological Survey (CGS), MOEA. (2021). Active fault map of Taiwan. Retrieved from https://faultnew.moeacgs.gov.tw/ckfinder/connector?command=Proxy%26type=Attach%26currentFolder=/%26fileName=2021%20Taiwan%20Fault%20Distribution%20Map%28English%20Version%29.jpg%26c=2%26p=tblAbout_1%26l=4

Champenois, J., Fruneau, B., Pathier, E., Deffontaines, B., Lin, K.-C., & Hu, J.-C. (2012). Monitoring of active tectonic deformations in the Longitudinal Valley (Eastern Taiwan) using persistent scatterer InSAR method with ALOS PALSAR data. *Earth and Planetary Science Letters*, *337–338*, 144–155. https://doi.org/10.1016/j.epsl.2012.05.025

Chan, C.-H., Ma, K.-F., Shyu, J. B. H., Lee, Y.-T., Wang, Y.-J., Gao, J.-C., et al. (2020). Probabilistic seismic hazard assessment for Taiwan: TEM PSHA2020. *Earthquake Spectra*, *36*(1_suppl), 137–159. https://doi.org/10.1177/8755293020951587

Chen, C.-T., Hu, J.-C., Lu, C.-Y., Lee, J.-C., & Chan, Y.-C. (2007). Thirty-year land elevation change from subsidence to uplift following the termination of groundwater pumping and its geological implications in the metropolitan Taipei basin, Northern Taiwan. *Engineering Geology*, *95*(1–2), 30–47. https://doi.org/10.1016/j.enggeo.2007.09.001

Chen, C. W., & Zebker, H. A. (2002). Phase unwrapping for large SAR interferograms: Statistical segmentation and generalized network models. *IEEE Transactions on Geoscience and Remote Sensing*, *40*(8), 1709–1719. https://doi.org/10.1109/tgrs.2002.802453

Chen, W.-S. (2016). *Introduction to Taiwan geology*. Geological Society. (p. 250).

Ching, K.-E., Hsieh, M.-L., Johnson, K. M., Chen, K.-H., Rau, R.-J., & Yang, M. (2011). Modern vertical deformation rates and mountain building in Taiwan from precise leveling and continuous GPS observations, 2000–2008. *Journal of Geophysical Research*, *116*(B8), B08406. https://doi.org/10.1029/2011JB008242

Elliott, J. R., Walters, R. J., & Wright, T. J. (2016). The role of space-based observation in understanding and responding to active tectonics and earthquakes. *Nature Communications*, *7*(1), 13844. https://doi.org/10.1038/ncomms13844

Farr, T. G., Rosen, P. A., Caro, E., Crippen, R., Duren, R., Hensley, S., et al. (2007). The shuttle radar topography mission. *Reviews of Geophysics*, *45*(2), RG2004. https://doi.org/10.1029/2005RG000183

Fattahi, H., Agram, P., & Simons, M. (2017). A network-based enhanced spectral diversity approach for TOPS time-series analysis. *IEEE Transactions on Geoscience and Remote Sensing*, *55*(2), 777–786. https://doi.org/10.1109/tgrs.2016.2614925

Hersbach, H., Bell, B., Berrisford, P., Hirahara, S., Horanyi, A., Munoz-Sabater, J., et al. (2020). The ERA5 global reanalysis. *Quarterly Journal of the Royal Meteorological Society*, *146*(730), 1999–2049. https://doi.org/10.1002/qj.3803

Hsu, L., & Bürgmann, R. (2006). Surface creep along the Longitudinal Valley fault, Taiwan from InSAR measurements. *Geophysical Research Letters*, *33*(6), L06312. https://doi.org/10.1029/2005GL024624

Hsu, Y.-J., Lai, Y.-R., You, R.-J., Chen, H.-Y., Teng, L. S., Tsai, Y.-C., et al. (2018). Detecting rock uplift across southern Taiwan mountain belt by integrated GPS and leveling data. *Tectonophysics*, *744*, 275–284. https://doi.org/10.1016/j.tecto.2018.07.012

Huang, M.-H., Bürgmann, R., & Hu, J.-C. (2016a). Fifteen years of surface deformation in southwestern Taiwan: Insight from SAR inter-ferometry. *Tectonophysics*, *692*, 252–264. https://doi.org/10.1016/j.tecto.2016.02.021

Huang, M.-H., & Evans, E. L. (2019). Total variation regularization of geodetically constrained block models in Southwest Taiwan. *Journal of Geophysical Research: Solid Earth*, *124*(12), 13269–13285. https://doi.org/10.1029/2019JB018076

Huang, M.-H., Hu, J.-C., Hsieh, C.-S., Ching, K.-E., Rau, R.-J., Pathier, E., et al. (2006). A growing structure near the deformation front in SW Taiwan as deduced from SAR interferometry and geodetic observation. *Geophysical Research Letters*, *33*(12), L12305. https://doi.org/10.1029/2005GL025613

Huang, M.-H., & Huang, H.-H. (2018). The complexity of the 2018 M_w 6.4 Hualien earthquake in east Taiwan. *Geophysical Research Letters*, *45*(13), 13–249. https://doi.org/10.1029/2018GL080821

Huang, M.-H., Tung, H., Fielding, E. J., Huang, H.-H., Liang, C., Huang, C., & Hu, J.-C. (2016b). Multiple fault slip triggered above the 2016 M_w 6.4 MeiNong earthquake in Taiwan. *Geophysical Research Letters*, *43*(14), 7459–7467. https://doi.org/10.1002/2016GL069351

Hung, W.-C., Hwang, C., Chang, C.-P., Yen, J.-Y., Liu, C.-H., & Yang, W.-H. (2010). Monitoring severe aquifer-system compaction and land subsidence in Taiwan using multiple sensors: Yunlin, the southern Choshui River Alluvial Fan. *Environmental Earth Sciences*, *59*(7), 1535–1548. https://doi.org/10.1007/s12665-009-0139-9

Hung, W.-C., Hwang, C., Chen, Y.-A., Chang, C.-P., Yen, J.-Y., Hooper, A., & Yang, C.-Y. (2011). Surface deformation from persistent scatterers SAR interferometry and fusion with leveling data: A case study over the Choushui River Alluvial Fan, Taiwan. *Remote Sensing of Environment*, *115*(4), 957–967. https://doi.org/10.1016/j.rse.2010.11.007

Le Béon, M., Marc, O., Suppe, J., Huang, M.-H., Huang, S.-T., & Chen, W.-S. (2019). Structure and deformation history of the rapidly growing Tainan anticline at the deformation front of the Taiwan mountain belt. *Tectonics*, *38*(9), 3311–3334. https://doi.org/10.1029/2019TC005510

Lee, J.-C., Angelier, J., Chu, H.-T., Hu, J.-C., & Jeng, F.-S. (2005). Monitoring active fault creep as a tool in seismic hazard mitigation. Insights from creepmeter study at Chihshang, Taiwan. *Comptes Rendus Geoscience*, *337*(13), 1200–1207. https://doi.org/10.1016/j.crte.2005.04.018

Lin, K.-C., Hu, J.-C., Ching, K.-E., Angelier, J., Rau, R.-J., Yu, S.-B., et al. (2010). GPS crustal deformation, strain rate, and seismic activity after the 1999 chi-chi earthquake in Taiwan. *Journal of Geophysical Research*, *115*(B7), B07404. https://doi.org/10.1029/2009JB006417

Rollins, C., & Avouac, J.-P. (2019). A geodesy- and seismicity-based local earthquake likelihood model for central Los Angeles. *Geophysical Research Letters*, *46*(6), 3153–3162. https://doi.org/10.1029/2018GL080868

Rosen, P. A., Gurrola, E., Sacco, G. F., & Zebker, H. (2012). The InSAR scientific computing environment. In *Proceedings of EUSAR* (pp. 730–733).

Shen, Z.-K., & Liu, Z. (2020). Integration of GPS and InSAR data for resolving 3-dimensional crustal deformation. *Earth and Space Science*, *7*(4), e2019EA001036. https://doi.org/10.1029/2019EA001036

Shyu, J. B., Yin, Y.-H., Chen, C.-H., Chuang, Y.-I., & Liu, S.-C. H. (2020). Updates to the on-land seismogenic structure source database by the Taiwan Earthquake Model (TEM) project for seismic hazard analysis of Taiwan. *Terrestrial, Atmospheric and Oceanic Sciences*, *31*(4), 469–478. https://doi.org/10.3319/TAO.2020.06.08.01

Shyu, J. B. H., Chuang, Y. R., Chen, Y. L., Lee, Y. R., & Cheng, C. T. (2016). A new on-land seismogenic structure source database from the Taiwan earthquake model (TEM) project for seismic hazard analysis of Taiwan. *Terrestrial, Atmospheric and Oceanic Sciences*, *27*(3), 311. https://doi.org/10.3319/tao.2015.11.27.02(tem)

Sudhaus, H., & Jónsson, S. (2009). Improved source modelling through combined use of Insar and GPS under consideration of correlated data errors: Application to the June 2000 Kleifarvatn earthquake, Iceland. *Geophysical Journal International*, *176*(2), 389–404. https://doi.org/10.1111/j.1365-246x.2008.03989.x

Teng, L. S., Lee, C.-T., Peng, C.-H., Chu, J.-J., & Chen, W.-F. (2001). Origin and geological evolution of the Taipei basin, northern Taiwan. *Western Pacific Earth Sciences*, *1*, 115–142.

Tong, X., Sandwell, D. T., & Smith-Konter, B. (2013). High-resolution interseismic velocity data along the San Andreas Fault from GPS and InSAR. *Journal of Geophysical Research: Solid Earth*, *118*(1), 369–389. https://doi.org/10.1029/2012jb009442

Tung, H., & Hu, J.-C. (2012). Assessments of serious anthropogenic land subsidence in Yunlin County of central Taiwan from 1996 to 1999 by persistent scatterers InSAR. *Tectonophysics*, *578*, 126–135. https://doi.org/10.1016/j.tecto.2012.08.009

Wang, Y.-J., Chan, C.-H., Lee, Y.-T., Ma, K.-F., Shyu, J. B. H., Rau, R.-J., & Cheng, C.-T. (2016). Probabilistic seismic hazard assessment for Taiwan. *Terrestrial, Atmospheric and Oceanic Sciences*, *27*(3), 325–340. https://doi.org/10.3319/TAO.2016.05.03.01(TEM)

Weiss, J. R., Walters, R. J., Morishita, Y., Wright, T. J., Lazecky, M., Wang, H., et al. (2020). High-resolution surface velocities and strain for anatolia from sentinel-1 InSAR and GNSS data. *Geophysical Research Letters*, *47*(17). https://doi.org/10.1029/2020gl087376

Yu, S.-B., Chen, H.-Y., & Kuo, L.-C. (1997). Velocity field of GPS stations in the Taiwan area. *Tectonophysics*, *274*(1-3), 41–59. https://doi.org/10.1016/S0040-1951(96)00297-1

Yunjun, Z., Fattahi, H., & Amelung, F. (2019). Small baseline InSAR time series analysis: Unwrapping error correction and noise reduction. *Computers & Geosciences*, *133*, 104331. https://doi.org/10.1016/j.cageo.2019.104331

References From the Supporting Information

Fagereng, Å., & Biggs, J. (2019). New perspectives on "geological strain rates" calculated from both naturally deformed and actively deforming rocks. *Journal of Structural Geology*, *125*, 100–110. https://doi.org/10.1016/j.jsg.2018.10.004

Hussain, E., Hooper, A., Wright, T. J., Walters, R. J., & Bekaert, D. P. (2016). Interseismic strain accumulation across the central North Anatolian Fault from iteratively unwrapped InSAR measurements. *Journal of Geophysical Research: Solid Earth*, *121*(12), 9000–9019. https://doi.org/10.1002/2016JB013108

Pagani, C., Bodin, T., Métois, M., & Lasserre, C. (2021). Bayesian estimation of surface strain rates from global navigation satellite system measurements: Application to the southwestern United States. *Journal of Geophysical Research: Solid Earth*, *126*(6), e2021JB021905. https://doi.org/10.1029/2021jb021905

Watson, A. R., Elliott, J. R., & Walters, R. J. (2022). Interseismic strain accumulation across the main recent fault, SW Iran, from Sentinel-1 INSAR Observations. *Journal of Geophysical Research: Solid Earth*, *127*(2), e2021JB022674. https://doi.org/10.1029/2021jb022674